

The structure of the cometary globule CG 12: a high-latitude star-forming region^{★,★★}

L. K. Haikala^{1,2} and M. Olberg³

¹ Observatory, PO Box 14, University of Helsinki, Finland
e-mail: haikala@astro.helsinki.fi

² Swedish-ESO Submillimetre Telescope, European Southern Observatory, Casilla 19001, Santiago, Chile

³ Onsala Space Observatory, 439 00 Onsala, Sweden
e-mail: michael.olberg@chalmers.se

Received 23 March 2006 / Accepted 22 September 2006

ABSTRACT

We have investigated the structure of the high galactic-latitude cometary globule 12 (CG 12) by means of radio molecular-line observations. Detailed, high signal-to-noise ratio maps in C¹⁸O (1–0), C¹⁸O (2–1) and molecules tracing high-density gas, CS (3–2), DCO⁺ (2–1), and H¹³CO⁺ (1–0), are presented. The C¹⁸O line emission is distributed in a 10′ long North-South elongated lane with two strong maxima, CG 12-N(orth) and CG 12-S(outh). In CG 12-S the high-density tracers delineate a compact core, DCO⁺ core, which is offset by 15″ from the C¹⁸O maximum. The observed strong C¹⁸O emission traces either the surface of the DCO⁺ core or a separate, adjacent cloud component. The driving source of the collimated molecular outflow detected in 1993 is located in the DCO⁺ core. The C¹⁸O lines in CG 12-S have low-intensity wings possibly caused by the outflow. The emission in high-density tracers is weak in CG 12-N and especially the H¹³CO⁺, DCO⁺, and N₂H⁺ lines are +0.5 km s^{−1} offset in velocity with respect to the C¹⁸O lines. Evidence is presented that the molecular gas is highly depleted. The observed strong C¹⁸O emission towards CG 12-N originates in the envelope of this depleted cloud component or in a separate entity seen in the same line of sight. The C¹⁸O lines in CG 12 were analysed using positive matrix factorization, PMF. The shape and the spatial distribution of the individual PMF factors fitted separately to the C¹⁸O (1–0) and (2–1) transitions were consistent with each other. The results indicate a complex velocity and line excitation structure in the cloud. Besides separate cloud velocity components the C¹⁸O line shapes and intensities are influenced by excitation temperature variations caused by e.g., the molecular outflow or by molecular depletion. Assuming a distance of 630 pc the size of the CG 12 compact head, 1.1 pc by 1.8 pc, and the C¹⁸O mass larger than 100 M_⊙ are comparable to those of other nearby low/intermediate mass star formation regions.

Key words. clouds – ISM molecules – ISM: structure – radio lines – ISM: individual objects: CG 12 – ISM: individual objects: NGC 5367

1. Introduction

Herschel (1847) noted that a 10th mag. star, now known as h4636 or CoD −39° 8581, is a binary with a separation of 3′.7. In the optical, h4636 illuminates the bright reflection nebula NGC 5367. Hawarden & Brand (1976) showed that it lies in the head of an impressive cometary globule 12, CG 12, with a tail stretching about one degree to the SE. With a galactic latitude of 21° and at the distance of 630 pc estimated by Williams et al. (1977), CG 12 lies more than 200 pc above the plane. It has an associated low/intermediate mass stellar cluster that has at least 9 members (Williams et al. 1977).

The cloud’s cometary structure could be due to the passage of a supernova blast wave. Curiously, the cometary tail stretches towards the Galactic plane, which would place the putative supernova even farther away from the Galactic plane than the globule. According to Maheswar et al. (1996), the head of CG 12 is pointing towards the centre of an HI shell. Such a shell is, however, not readily evident in the whole-sky HI survey (Kalberla et al. 2005), which merges the northern

Leiden/Dwingeloo Survey (Hartman & Burton 1997) and the southern Instituto Argentino de Radioastronomia Survey (Arnal et al. 2000). The CG 12 cloud cometary shape is also seen in the IRAS surface emission (Odenwald 1988).

White (1993) mapped the region around and south of h4636 in ¹²CO (2–1) and C¹⁸O (2–1) lines with a spatial resolution of 22″. He found a small C¹⁸O core near the binary and a molecular outflow with a centre close to the binary system. Further large-scale ¹²CO, ¹³CO, and C¹⁸O observations with 2′.7 resolution are presented in Yonekura et al. (1999). CG 12 contains two compact 1.2 mm continuum sources, one in the direction of the C¹⁸O core detected by White (1993) (Reipurth et al. 1996) and another one two arcminutes north of it (Haikala 2007, in preparation). The centres of the continuum sources were observed in C¹⁸O (3–2) by Haikala et al. (2006).

Near-infrared (*J*, *H*, and *K*) images and photometry of stars in CG 12 are available in the 2MASS survey and in Santos et al. (1998). A deeper *J*, *H*, and *Ks* imaging study is presented in Haikala (2007, in preparation). Far-infrared emission in CG 12 is dominated by a strong point source, IRAS 13547-3944, near the binary h4636.

* Based on observations collected at the European Southern Observatory, La Silla, Chile.

** Figures 11 and 12 and Appendix A are only available in electronic form via <http://www.aanda.org>

CG 12/NGC 5367 is an intriguing object. It has the appearance of a cometary globule such as usually found on the outskirts of HII regions. The linear size of cometary globules, like those in the Gum nebula, are however much smaller (e.g., Reipurth 1983). The linear extent of CG 12, 10 pc, is four times larger than, e.g., the archetype object CG 1. A low/intermediate mass stellar cluster is associated with CG 12. Perhaps the most curious feature of CG 12 is its location over 200 pc above the Galactic plane with no sign of other nearby dark clouds or star formation. CG 12 has not attracted much interest since the identification of the stellar cluster (Williams et al. 1977) and the Hawarden & Brand (1976) cometary globule paper. Subsequent papers have either concentrated on the Herbig AeBe binary, h4636, or the cloud has been included in various surveys. The ^{12}CO (2–1) and C^{18}O (2–1) observations by White (1993), though detailed, cover only the very centre of the cloud. What has been missing is a detailed, but at the same time extended, study of the dense CG 12 molecular cloud in molecular transitions that are sensitive to the large-scale structure (cloud envelope) and to the detailed structure of the high-density material (cores).

In this paper we report the mapping of the head of CG 12 in the C^{18}O (1–0) and (2–1) and in ^{13}CO (1–0) lines. The C^{18}O emission maxima were further mapped in DCO^+ (2–1), H^{13}CO^+ (1–0), and CS (2–1) and (3–2). More pointed observations with a long integration time in CO (1–0) and (2–1) (and isotopologues), CS (2–1) and (3–2), C^{34}S (2–1), H^{13}CO^+ (1–0), DCO^+ (2–1), and N_2H^+ (1–0) were made towards selected positions in the cloud.

Observations, data reduction, and calibration procedures are described in Sect. 2 and the observational results in Sect. 3. The new results are compared with the optical and NIR images in Sect. 4. In Sect. 5 and Appendix A, PMF is used to analyse the C^{18}O small-scale structure in the globule. In the discussion part in Sect. 6, the C^{18}O column densities and the cloud mass are derived and the observational and calculated results are summarised. The conclusions are drawn in Sect. 7.

2. Observations

The observations were made during various observing runs with the Swedish-ESO-Submillimetre-Telescope, SEST, at the La Silla observatory, Chile. The SEST 3 mm dual polarization, single sideband (SSB), Schotky receiver was used for the ^{13}CO (1–0) and CS (2–1) mapping observations. The rest of the observations were conducted with the SEST 3 and 2 mm (SESIS) and 3 and 1 mm (IRAM) dual SiS SSB receivers. The SEST high-resolution, 2000-channel acousto-optical spectrometer (bandwidth 86 MHz, channel width 43 kHz) was split into two halves to measure two receivers simultaneously. At the observed wavelengths, 3 mm, 2 mm, and 1 mm, the 43 kHz channel width corresponds to $\sim 0.12 \text{ km s}^{-1}$, $\sim 0.08 \text{ km s}^{-1}$, and $\sim 0.06 \text{ km s}^{-1}$, respectively.

Frequency-switching observing mode was used and a second-order baseline was subtracted from the spectra after folding. Calibration was achieved by the chopper wheel method. All the line temperatures in this paper, if not especially noted, are in the units of T_A^* , i.e. corrected to outside of the atmosphere but not for beam coupling. Typical values for the effective SSB system temperatures outside the atmosphere ranged from 200 K to 350 K. Pointing was checked regularly in continuum mode towards the nearby Centaurus A galaxy and the pointing accuracy is estimated to be better than $5''$.

The observed molecular transitions, their frequencies, SEST half power beam width, *HPBW*, and the telescope main beam

Table 1. Observed lines and telescope parameters.

Line	ν [GHz]	<i>HPBW</i> [']	η_{mb}
H^{13}CO^+ (1–0)	86.754	57	0.75
N_2H^+ (1–0)	93.176	54	
C^{34}S (2–1)	96.412	54	
CS (2–1)	97.271	54	
C^{18}O (1–0)	109.782	47	0.70
DCO^+ (2–1)	144.077	34	
CS (3–2)	145.904	34	0.66
C^{18}O (2–1)	219.560	24	0.50

efficiency, η_{mb} , at these frequencies are given in Table 1. For the CO observations only the C^{18}O is listed. At a distance of 630 pc the SEST *HPBW* at 219 GHz corresponds to 0.07 pc.

The cloud was mapped simultaneously in C^{18}O (1–0) and C^{18}O (2–1) transitions with a spacing of $20''$ (514 positions). The map central position was $13^{\text{h}}57^{\text{m}}43^{\text{s}}.1, -39^{\circ}58'43''.3$ (J2000), which is $-5''$ and $\sim -10''$ in right ascension from the positions of the IRAS 13547-3944 point source and the binary h3626, respectively. The average rms of the spectra were 0.07 K and 0.09 K for C^{18}O (1–0) and (2–1), respectively. An approximately $8'$ by $20'$ area was mapped in ^{13}CO using $40''$ spacing (324 positions). The C^{18}O maxima were mapped in CS (2–1), (3–2), DCO^+ (2–1), and H^{13}CO^+ (1–0). Further long integration time pointed observations in CO, CS, H^{13}CO^+ , DCO^+ , C^{34}S , and N_2H^+ were made.

3. Results

The mapping of CG 12 in C^{18}O and in molecules tracing high-density material provides a large-scale view of the cloud. High signal-to-noise spectra in selected molecular transitions were obtained by pointed observations with a long integration time. These spectra probe the cloud at different depths and densities. Combining the intensity and velocity information in the pointed spectra provides a clue to the cloud fine-scale structure.

3.1. CO

The observed distributions of C^{18}O (1–0) and C^{18}O (2–1) line emission towards CG12 are presented in Fig. 1 (the $\int T_A^* dv$ in the velocity range -8 km s^{-1} to -4 km s^{-1}) and Figs. 11 and 12 (C^{18}O channel maps). In the figures the grey/colour scales and the contour levels are the same for the two C^{18}O transitions. The offsets from the map centre position in arc minutes are shown on the axes of the right panel in Fig. 1.

The bulk of the molecular material traced by C^{18}O emission is distributed in a narrow North-South oriented lane with two prominent maxima. A less intense maximum is observed to the SW. Henceforth the three intensity maxima will be referred to as CG 12-N, CG 12-S, and CG 12-SW, where CG 12-S corresponds to the C^{18}O (2–1) maximum reported in White (1993).

The morphology of the cloud is similar in the two C^{18}O transitions. However, there is a notable difference between the C^{18}O maxima. The observed C^{18}O (1–0) emission is stronger than the C^{18}O (2–1) emission in CG 12-N and CG 12-SW, whereas in CG 12-S the opposite is the case. In CG 12-N the C^{18}O (1–0) line remains stronger than the (2–1) line even when expressed on the main beam brightness-temperature scale.

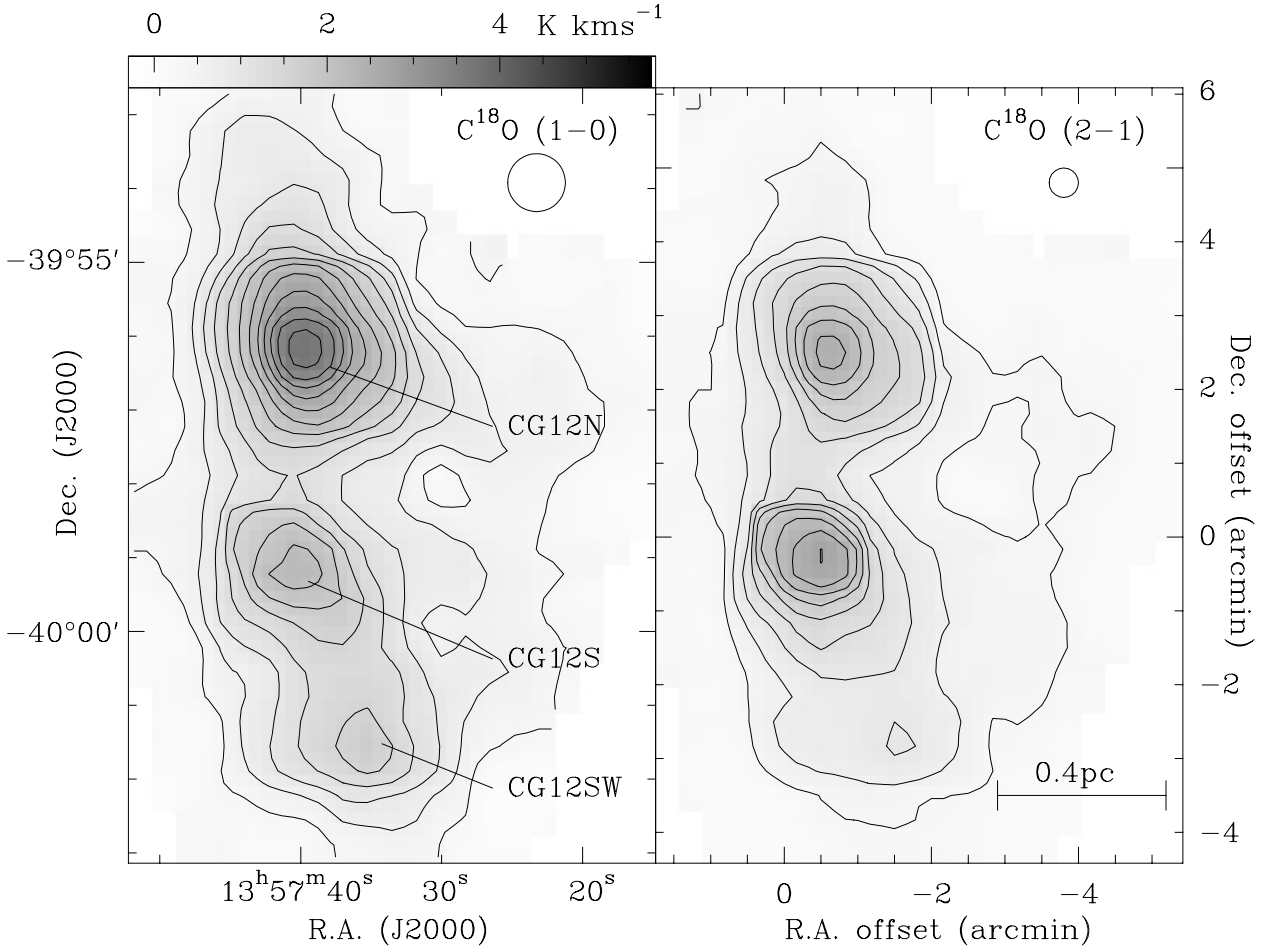


Fig. 1. Maps of integrated emission of C^{18}O (1–0) and C^{18}O (2–1) $\int T_{\text{A}}^* dv$ from -8 km s^{-1} to -4 km s^{-1} in CG12. The lowest contour and the contour increment are 0.3 K km s^{-1} . The SEST half-power beam sizes are shown in the upper corners of the panels. Offsets from the map’s central position, $13^{\text{h}}57^{\text{m}}43^{\text{s}}.1$, $-39^{\circ}58'43''.3$ (J2000), are shown on the axes of the right panel. The scale tick in the lower right corner assumes a distance of 630 pc to the cloud.

More details can be seen in Figs. 11 and 12, which reveal that the structure of the cloud is not as simple as Fig. 1 suggests. The most noticeable features are the following: CG 12-N is elongated in the North South direction at velocities $\leq -6.0 \text{ km s}^{-1}$ and in the East West direction at velocities $\geq -5.4 \text{ km s}^{-1}$. The position of the maximum C^{18}O (2–1) emission in CG 12-S moves from below the map centre position (marked with a cross in the figure) at -7.0 km s^{-1} to a position $40''$ west of this position at velocity -5.9 km s^{-1} . An arc-like feature connects CG 12-S and CG 12-SW at velocities from -6.6 km s^{-1} to -6.2 km s^{-1} . The arc is less pronounced in the C^{18}O (2–1) transition.

The observed distribution of the ^{13}CO (1–0) line emission towards CG12 is presented in Fig. 2. The extent of the C^{18}O mapping and the outline of the C^{18}O (2–1) emission is indicated in the overlay. The notable difference between the observed C^{18}O and ^{13}CO emission is that there is only one ^{13}CO maximum, which is offset to NE from CG 12-S. In particular, there is no indication of CG 12-N on the ^{13}CO map.

The ^{12}CO , ^{13}CO , and C^{18}O (1–0) and (2–1) (pointed, long integration time) spectra in five selected positions in the cloud are shown in Fig. 3. The ^{12}CO spectra observed at all positions in the figure are strongly self-absorbed. Therefore the ^{12}CO line peak intensity, line half width, and the line integral are not physically meaningful. Line wing emission due to a molecular outflow (White 1993) is seen in all ^{12}CO spectra, also in the

direction of CG 12-N, which was not covered by the White (1993) observations.

3.2. high-density tracers, mapping

In the optically thin case the critical density of the C^{18}O (1–0) transition is $\sim 650 \text{ cm}^{-3}$ and approximately ten times this value for the (2–1) transition (Rohlfs & Wilson 1999). These C^{18}O lines are therefore already excited at low densities, and their emission traces column density rather than number density. Therefore the C^{18}O intensity maxima were also mapped in the high-density tracers (critical densities larger than 10^5 cm^{-3}) CS (2–1), H^{13}CO^+ (1–0) and DCO^+ (2–1) using $20''$ spacing. A 4 by 4 point map with the same spacing was obtained for CG 12-S in the CS (3–2) line.

Contour maps of the CS (2–1), CS (3–2), H^{13}CO^+ , and DCO^+ line integral in CG 12 superposed on the C^{18}O (2–1) emission (grey scale) are shown in Fig. 4. CG 12-N was not mapped in CS (3–2). The CS (2–1) emission peaks at the position of the C^{18}O (2–1) the maximum in CG 12-S. In other molecules the maximum is shifted to SE from the C^{18}O maximum. As DCO^+ traces high-density gas, the CG 12-S DCO^+ maximum will be referred to as the DCO^+ core.

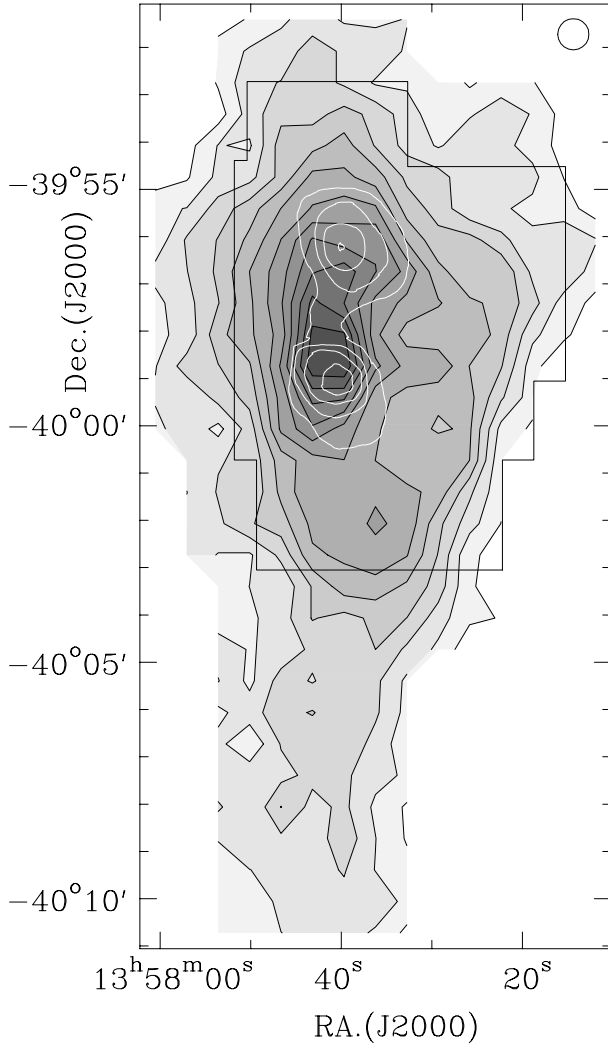


Fig. 2. Map of integrated emission of ^{13}CO (1-0): $\int T_{\text{A}}^* dv$ from -8 km s^{-1} to -4 km s^{-1} . The lowest contour and the contour increment are 1.2 K km s^{-1} . The SEST half-power beam size at the line frequency is shown in the upper corner. The extent of the C^{18}O mapping and the outline of the C^{18}O (2-1) emission is indicated in the overlay.

3.3. C^{18}O and high-density tracers: pointed observations

Pointed, long-integration-time CS (2-1), (3-2), C^{34}S (2-1), H^{13}CO^+ (1-0), DCO^+ (2-1), and N_2H^+ (1-0) spectra in the same positions as in Fig. 3 are shown in Fig. 5. The integration time of the CS (3-2) line at position $(-40'', -20'')$ is only 2.5 min and is therefore noisier than the two other CS (3-2) lines. The N_2H^+ (1-0) line consists of seven hyperfine components, and only the unblended N_2H^+ (1-0) ($F_1, F = 0, 1 \rightarrow 1, 2$) component is shown in Fig. 5.

The C^{34}S line was observed in three positions. These spectra together with the CS (2-1) and (3-2) spectra observed at the same positions are shown in Fig. 6. The N_2H^+ spectra showing all the hyperfine components in the three observed positions are shown in Fig. 7. Also the hyperfine component fits (assuming optically thin emission and one velocity component) and their residuals are shown.

3.3.1. CG 12-S

Near the centre of the DCO^+ core (position $-20'', -20''$), the H^{13}CO^+ , DCO^+ and N_2H^+ lines are nearly symmetric and centred at velocity -6.5 km s^{-1} . The C^{18}O lines are skewed and the maximum intensity is redshifted from the DCO^+ (2-1) peak velocity. Going to the West (position $-40'', -20''$) the redshifted side of the C^{18}O lines becomes more intense. Low-intensity wing-like emission is observed in the C^{18}O and CS (2-1) lines in the direction of the DCO^+ core and position $(0'', 0'')$.

The N_2H^+ line in the position $(-20'', -20'')$, can be fit with a single velocity component centred at -6.56 km s^{-1} (Fig. 7, lower panel). Due to the 0.73 km s^{-1} line half width, the hyperfine components are blended and the hyperfine structure is only marginally resolved. The signal-to-noise ratio of the spectrum is not sufficient to meaningfully fit the line total optical depth, τ_{tot} . The estimated τ_{tot} upper limit in this position is 5.

3.3.2. CG 12-N

In CG 12-N (position $-40'', 160''$), the C^{18}O lines are nearly symmetric but not Gaussian. The emission from the high-density tracers is weak when compared to what is observed in CG 12-S.

The C^{34}S line was observed in two positions in CG 12-N (Fig. 6). The CS(2-1) and (3-2) line profiles in these positions are not Gaussian and may be composed of two or three components. The peak intensity of the C^{34}S (2-1) line is redshifted with respect to the peak of the CS (3-2) line, which itself is redshifted with respect to the CS (2-1) line, which peaks approximately at the same velocity as the C^{18}O lines.

The observed ionic lines (DCO^+ (2-1), H^{13}CO^+ (1-0), and N_2H^+ (1-0)) are offset $+0.5 \text{ km s}^{-1}$ in velocity with respect to the C^{18}O lines and peak at a velocity where especially the C^{18}O (2-1) line intensity is low.

The N_2H^+ (1-0) line was observed in the same two positions as C^{34}S . In contrast to the CS lines, the observed N_2H^+ lines are identical within the noise (Fig. 7, two upper panels). The SEST beam is the same at CS (2-1) and N_2H^+ (1-0) frequencies. A hyperfine component fit to the CG 12-N N_2H^+ lines gives a 0.65 km s^{-1} broad line at -5.41 km s^{-1} . The estimated τ_{tot} upper limit in position $(-40'', -160'')$ is 2.

To rule out the observed intensity/velocity structure described above being due to calibration, pointing, or frequency setting problems, the observations were carefully checked by observing the C^{18}O and the DCO^+ , H^{13}CO^+ and CS lines one after the other and making pointing checks before and after observations. Also, e.g., the line pair DCO^+ (2-1) and C^{18}O (1-0) could be observed simultaneously with a dual receiver, thus excluding relative pointing errors.

4. Comparison with observations at other wavelengths

The C^{18}O (2-1) contour map superposed on the blue SERC-J DSS image is shown in Fig. 8. The bright optical reflection nebula NGC 5367 lies in front of CG 12-S, whereas CG 12-N is in the direction of an optically heavily-obscured region that is clearly seen in the inset. A 1.2 mm source (Haikala 2007, in preparation) coincides with the position of the CG 12-N C^{18}O maximum.

A Ks band image (Haikala 2007, in preparation) of CG 12 is shown in Fig. 9. Superposed on the image are the contours of the ^{12}CO (2-1) molecular-outflow line-wing emission (White 1993). In the insets, the C^{18}O (2-1) and DCO^+

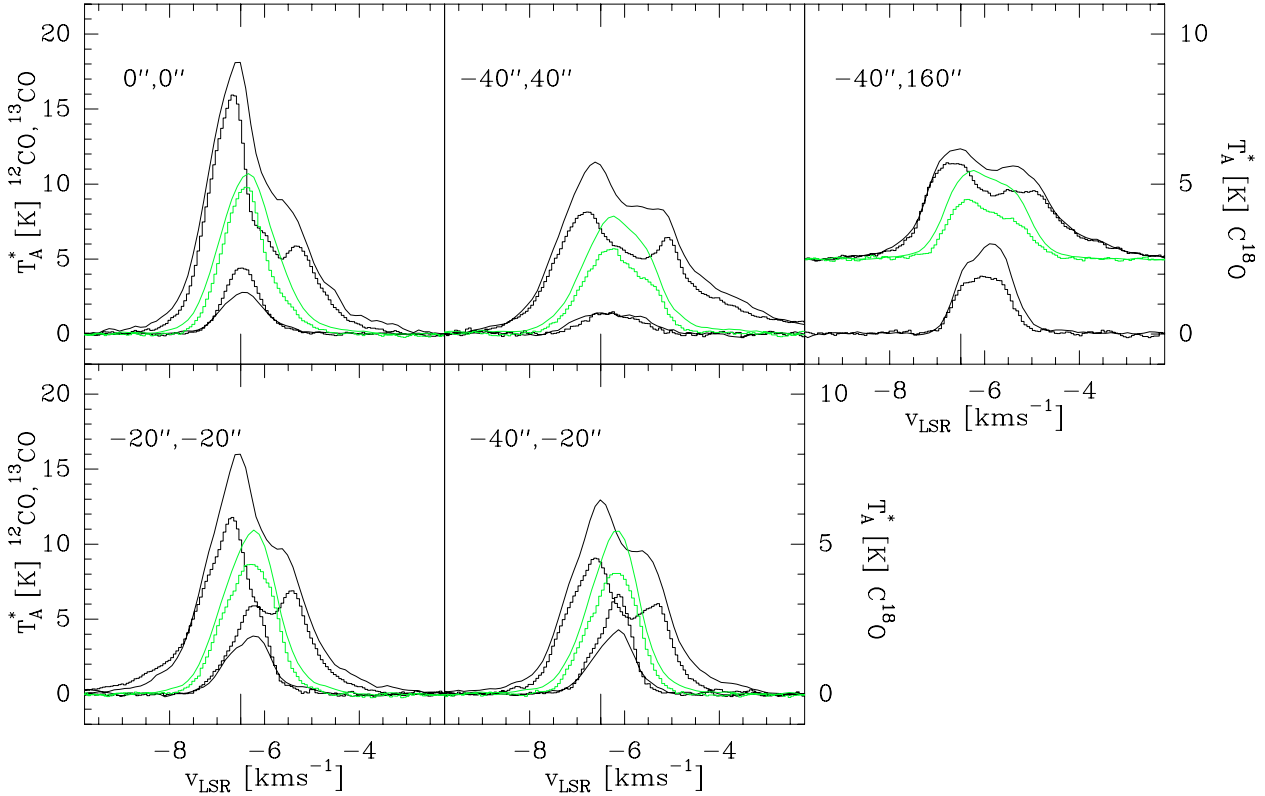


Fig. 3. ^{12}CO , ^{13}CO , and C^{18}O spectra observed towards five selected positions in CG 12. The offset from the map centre position is shown in arc seconds in the upper left corners of each panel. A line has been used for the (1–0) and a histogram for the (2–1) transitions. The antenna temperature scale at left is for ^{12}CO and ^{13}CO spectra and the one on the right for C^{18}O . The velocity tick indicates a velocity of -6.5 km s^{-1} . The ^{12}CO and ^{13}CO spectra in position $(-40'', 160'')$ are offset from the zero level for clarity.

contour maps are superposed, together with the positional uncertainty ellipses of IRAS point sources IRAS 13546-3941 and IRAS 13547-3944. IRAS 13547-3944 does not coincide with the binary h4636. The base of the binary star emission is saturated due to the intensity scale which was chosen to emphasize the low intensity surface emission.

A cone-like nebulosity with a bright head is seen projected on the DCO^+ core in Fig. 9. The apex of the cone is located just off the tip of the red shifted and below the end of the blue shifted, collimated CO outflow lobes of White (1993). A compact 1.2 mm source (Haikala 2007, in preparation) coincides with the DCO^+ core. The core does not have an associated point source, but this could be due to the low spatial resolution of the IRAS satellite. A faint source would be masked by the strong nearby source IRAS 13547-3944. The NIR cone could be associated with the driving source of the outflow. The centre of the molecular outflow is offset from the position of IRAS 13547-3944 by $\sim 20''$. It is unlikely that the point source is associated with the large outflow, but it could be the driving force for the strong redshifted outflow lobe located $\sim 1'$ NW of the nominal position of the point source.

Small areas of the size of the SEST *HPBW* at the C^{18}O (1–0) frequency in the centres of CG 12-N and CG 12-S have been mapped in the C^{18}O (3–2) (Haikala et al. 2006). The *HPBW* of the C^{18}O (3–2) observations is $19''$, which is similar to the SEST *HPBW* of $24''$ at the C^{18}O (2–1) frequency. In CG 12-S, the C^{18}O (3–2) emission has a strong maximum in the same position as the maxima in the lower C^{18}O transitions. The line profile in position $(-20'', -20'')$ agrees with the C^{18}O (2–1) line (Fig. 5). The C^{18}O (3–2) T_{MB} peak line temperature in this position is, however, 10 K, which is nearly twice the

C^{18}O (2–1) T_{MB} of 5.7 K. In CG 12-N (position $(-40'', 160'')$), the C^{18}O (3–2) line profile is similar to that of C^{18}O (1–0), but the T_{MB} peak line temperature is 3 K, which is lower than the corresponding values observed in C^{18}O (1–0) and (2–1), which are 4.3 K and 3.8 K, respectively.

5. C^{18}O fine-scale structure

The half widths of the observed C^{18}O lines in CG 12 cores range from 1.0 km s^{-1} (CG 12-S) to 1.3 km s^{-1} (CG 12-N). The C^{18}O channel-maps (Figs. 11 and 12) and observations of other molecules indicate that the lines consist of more than one velocity component. This division of the cloud according to its appearance in the C^{18}O line integral maps (Fig. 1) into only three components CG 12-N, CG 12-S, and CG 12-SW is therefore too coarse. The fine structure within the individual maxima is not seen because the lines are heavily blended in velocity.

5.1. Positive matrix factorization

Positive matrix factorization (PMF) has been used by Juvela et al. (1996) and Russeil et al. (2003) in the analysis of molecular line spectral maps. It assumes that the ensemble of input spectra are composed of n individual line components (factors). Unlike principal component analysis PMF assumes that the individual components are positive. This makes the interpretation of the results more straightforward than in principal component analysis where the results may contain negative components. No other assumptions are made for the shape of the factors. Each input spectrum can be reconstructed from the n PMF output factors by multiplying each factor by the weight assigned to it by PMF

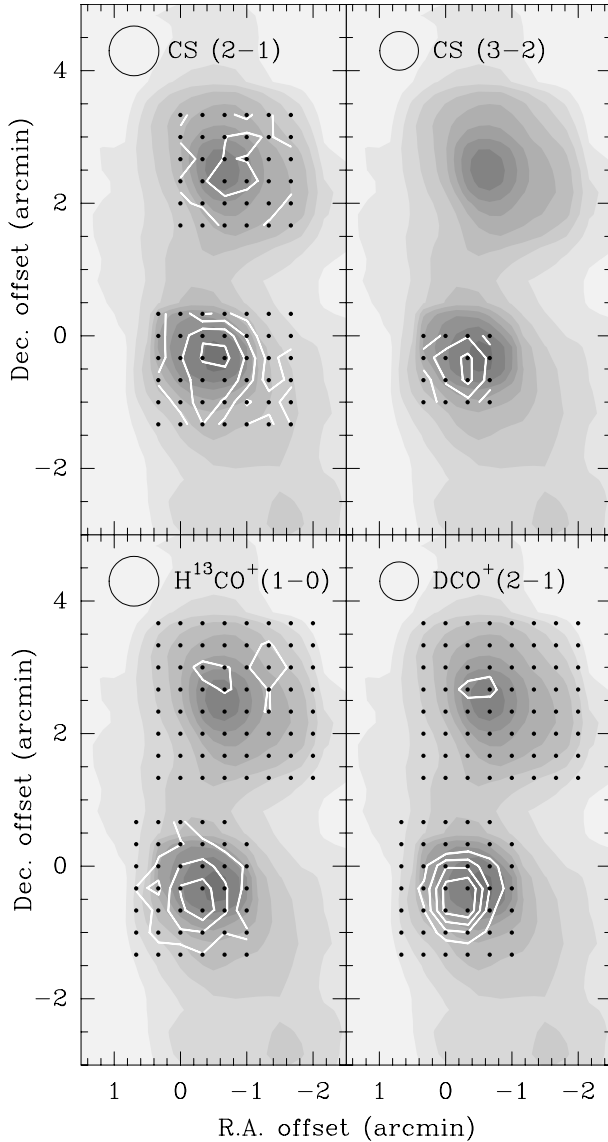


Fig. 4. Contour maps of the observed CS (2–1), CS (3–2), $\text{H}^{13}\text{CO}^+(1-0)$, and $\text{DCO}^+(2-1)$ distributions in CG 12 superposed on a grey-scale map of the C^{18}O (2–1) emission. The positions observed in each molecule are indicated. The corresponding SEST beam size at the observed frequencies is indicated in the upper left corner of each panel. In the CS (2–1) and CS (3–2) maps the lowest contour value is 0.5 K km s^{-1} and the increments are 0.5 K km s^{-1} and 0.3 K km s^{-1} , respectively. In the $\text{H}^{13}\text{CO}^+(1-0)$ and $\text{DCO}^+(2-1)$ maps, the lowest contour value and its increments are 0.15 K km s^{-1} . The maximum values of the CS (2–1), CS (3–2), $\text{H}^{13}\text{CO}^+(1-0)$, and $\text{DCO}^+(2-1)$ emission are 2.2 K km s^{-1} , 1.3 K km s^{-1} , 0.58 K km s^{-1} , and 0.77 K km s^{-1} , respectively. The offset from the map zero position is shown on the axes.

at the position and adding up the multiplied factors. A comparison of the results obtained with PMF analysis to those obtained using the analysis of channel maps and by the use of principal component analysis is given Russeil et al. (2003).

PMF has been applied separately to the north and south parts of CG 12, but there is a small positional overlap between the two areas used in the analysis. The same dataset, shown in Fig. 12, was used in the analysis, i.e., the C^{18}O (2–1) data is binned to the same channel width as the C^{18}O (1–0) data. The PMF analysis is presented in Appendix A.

6. Discussion

The interpretation of the C^{18}O data is not as straightforward as one would like and the possible caveats must be considered. The PMF fit to the observed C^{18}O data is good, but which part of the cloud material do the PMF factors trace? The structure of CG 12 and the physical properties of the associated gas can be estimated if the result of the PMF analysis is considered, together with the observed emission from molecules tracing high-density material.

6.1. C^{18}O as a tracer of molecular material

C^{18}O emission is generally considered a good tracer of the large-scale structure of dark clouds and globules. However, C^{18}O photodissociation in the cloud envelopes and molecular depletion in the dense and cold cloud cores may restrict the number density interval where C^{18}O emission can be used as a direct measure of H_2 column density (especially if the LTE approximation is used). Unlike ^{12}CO , the C^{18}O molecules are not shielded against photodissociation by strong H_2 lines, and furthermore, the C^{18}O self-shielding is weaker than that of ^{12}CO . For C^{18}O the self-shielding is most efficient for the two lowest rotational levels with the largest populations. According to Warin et al. (1996), the consequence is that the $J = 1-0$ transition becomes thermalized, whereas the higher transitions remain subthermally excited in the cloud envelopes. At the other extreme (pre-stellar cloud cores and protostellar envelopes), the CO molecule may vanish from the gas phase because of depletion onto dust grains. Other complications in interpreting C^{18}O data are the possible strong gradients in the CO excitation temperature on the line of sight due to heating of the gas by newly born stars and protostellar objects. Time and temperature dependent chemistry, such as deuterium fractionation, also complicates the comparison of C^{18}O data with that of other molecular species.

The depletion of molecules on dust grains takes place in the dense, quiescent, and cold molecular cloud cores. The CO and CS molecules are among the first to disappear from the gas phase, but nitrogen-bearing species, such as N_2H^+ and ammonia, seem to be able to resist depletion (Tafalla et al. 2002). The N_2H^+ and DCO^+ lines in CG 12-N peak at a velocity of 5.4 km s^{-1} where the C^{18}O line emission is weak (Sect. 3.3). It is likely that strong CO depletion has taken place in the gas traced by these two molecules in CG 12-N.

In CG 12-S the C^{18}O maximum is spatially offset from the DCO^+ core. Deuterium fractionation reactions are favoured in cold gas (e.g., Herbst 1982), so the relative abundance of DCO^+ is enhanced in cold cloud cores. The relatively strong DCO^+ emission observed in CG 12-S, the DCO^+ core, could indicate that fractionation has indeed taken place. If the molecules in CG 12-S were heavily depleted in the cold DCO^+ core, one would not expect CS (3–2) or H^{13}CO^+ to outline the core like they do (also DCO^+ will be finally depleted).

The observed ^{12}CO (1–0) and (2–1) line temperatures in CG 12-S (Fig. 3) are high. The lines are self reversed, so the actual line peak temperatures must be even higher. This indicates that the CO excitation temperature is in excess of 30 K in the part of the cloud that is traced by the observed ^{12}CO emission. White (1993) suggests that either h4636 or IRAS 13547-3944 is the heating source. The ^{12}CO and ^{13}CO optical depth is high and, unlike C^{18}O , these CO isotopologues are likely to trace only the surface of the molecular cloud associated with CG 12. The observed C^{18}O (3–2) T_{MB} peak temperature of 11 K

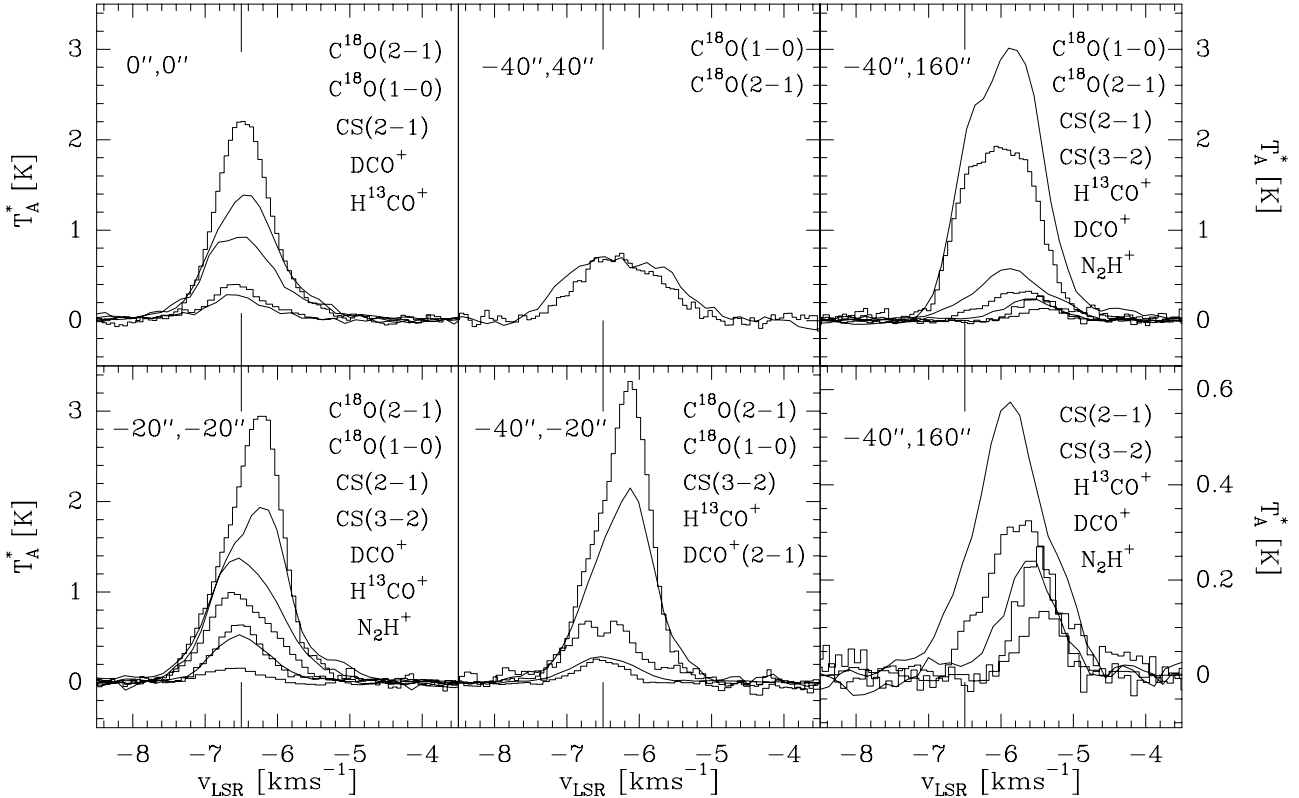


Fig. 5. Spectra of the $C^{18}O$ and molecules that are sensitive to number density towards the same positions as shown in Fig. 3. Only the unblended hyperfine N_2H^+ (1-0) ($F, F = 1, 0 \rightarrow 1, 2$) component is shown. The velocity tick indicates a velocity of -6.5 km s^{-1} . The $C^{18}O$ (1-0), CS (2-1) and $H^{13}CO^+$ lines are plotted using a continuous line. The panel lower right is a blowout of the upper right panel showing only the lines tracing high number density.

in CG 12-S also points at a high $C^{18}O$ excitation temperature (Haikala et al. 2006). However, the observed relative $C^{18}O$ (2-1) and (1-0) line intensities in CG 12-S are not compatible with $C^{18}O$ T_{ex} values higher than 20 K.

6.2. PMF: the interpretation

One should be cautious in interpreting the PMF results. Even though the fit to the $C^{18}O$ (1-0) and (2-1) data is good, all the PMF factors do not necessarily describe real cloud components. The structure of the cloud can, however, be discussed with some confidence when the PMF fit results are considered with the information provided by other available molecular lines, mm-continuum, and NIR-FIR data.

6.2.1. CG 12-S

The location of the CG 12-S $C^{18}O$ (2-1) PMF factor maxima relative to the NIR cone (and the mm continuum source) in the centre of the DCO^+ core is shown in Fig. 10. From East to West the factors are 1s, 2s, and 3s. The centres of the maxima differ in position by about one SEST beam size at 220 GHz, $24''$.

The data would seem to imply that CG 12-S is fragmented into three individual cores. If this were the case, one would expect that the 2s factor would coincide with the DCO^+ core because the 2s centre of line velocity is the same as that of DCO^+ . Even though the 3s factor is the strongest in CG 12-S, it is detected only as an asymmetry in the DCO^+ and CS lines in Figs. 5 and 6. CO is ubiquitous and easily excited, so that it can be detected at much lower densities than the high-density tracers

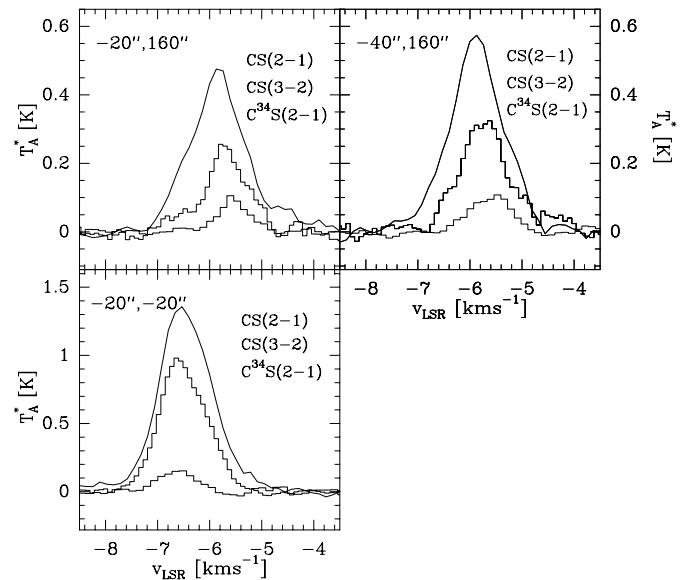


Fig. 6. CS (2-1), (3-2) and $C^{34}S$ (1-0) spectra observed in the direction of CG 12-N (the two upper panels) and CG 12-S (the lower panel).

DCO^+ and CS (3-2), which trace the DCO^+ core. The bulk of the observed $C^{18}O$ emission may have its origin in that part of the cloud where the density is lower and the excitation temperature higher than in the DCO^+ core.

This leads to a model where most of the observed $C^{18}O$ emission instead traces either the surface of the dense and cold cloud core (the DCO^+ core) or a separate, adjacent cloud

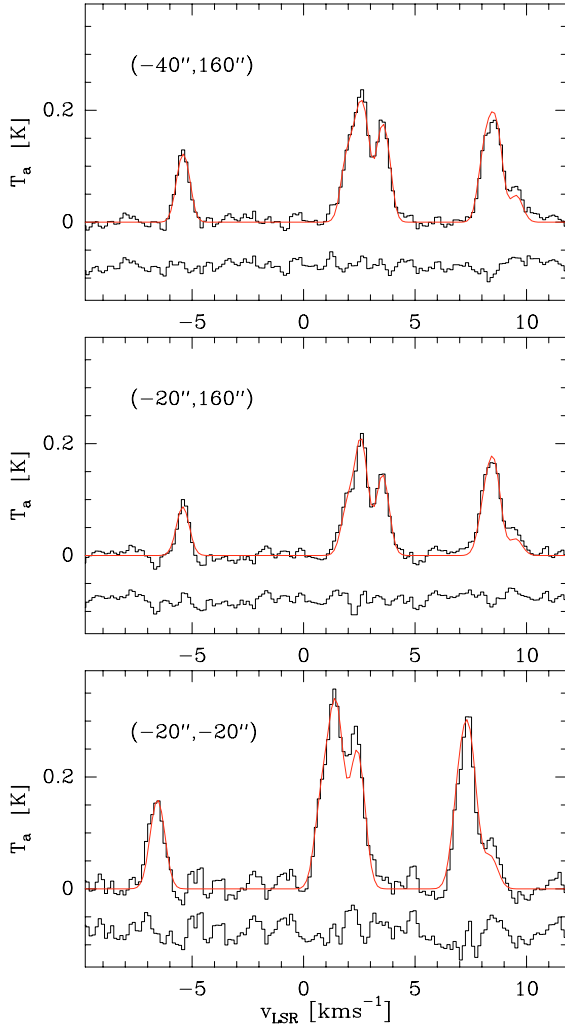


Fig. 7. N_2H^+ (1–0) spectra observed in the direction of CG 12-N (the two upper panels) and CG 12-S (the lower panel). The seven-component hyperfine structure fit and the resulting residuals are shown.

component, rather than the core itself. The observed CS (2–1) distribution, which is similar to C^{18}O in CG 12-S (Fig. 4), is in accord with this model. Much of the observed CS (2–1) emission is known to originate in cloud envelopes and not in the dense cores. The CS (3–2) effective critical density is higher than that of CS (2–1), therefore it traces the dense gas deeper in the cloud than CS (2–1).

The possible interaction of the collimated molecular outflow detected by White (1993) with the cloud core further complicates the interpretation of the molecular line data. The centre of the outflow is located in the direction of the DCO^+ core, and it is not unlikely that the outflow can produce weak C^{18}O line wings and that it can raise the CO excitation temperature locally. Weak line wings are also observed in the CS (2–1) line in Fig. 5. It is argued that the weak C^{18}O red and blue shifted line wing emission near the DCO^+ core is produced by the interaction of the collimated molecular outflow with the parent cloud. The line wings would be described by the PMF factors 1s and 4s. For the latter factor this would consist only of the emission immediately to the west of the DCO^+ core.

The CG 12-S C^{18}O (3–2) map in Haikala et al. (2006) covers only the very centre of CG 12-S. The C^{18}O (3–2) line peak velocity and the intensity distribution is in accordance with the elongated shape of the 3s component in Fig. 10. The maximum

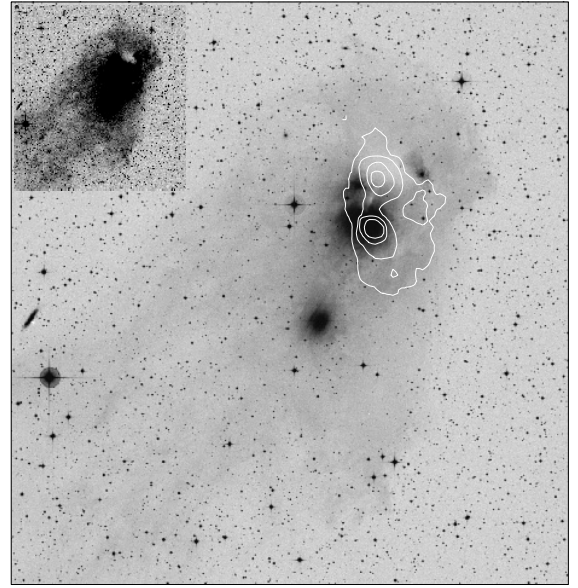


Fig. 8. Contour map of the C^{18}O (2–1) emission superposed on the optical (DSS blue) image of NGC 5367. The image is also shown in the inset but using an intensity scale that brings out the surface emission better. The linear size of the image is 32' by 32'.

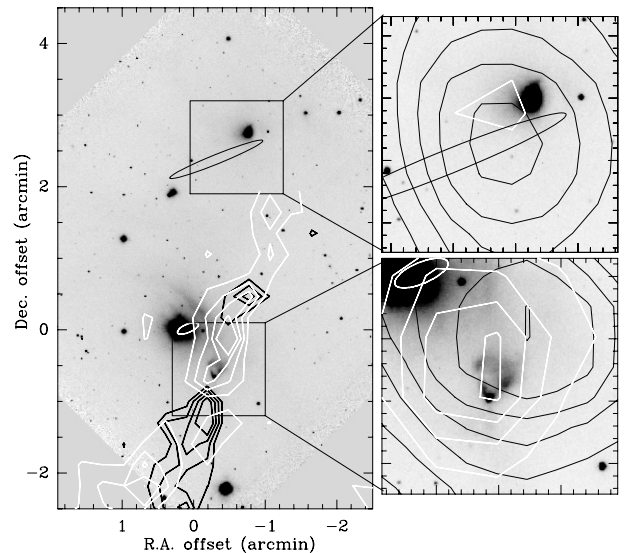


Fig. 9. Ks-band image of CG-12 (Haikala 2007, in preparation). Contours of the blue (white contours) and redshifted (black) ^{12}CO (2–1) line-wing emission (White 1993) are also shown. The two insets show the CG 12-S and CG 12-N regions in detail. Superposed are the contours of C^{18}O (2–1) (black) and DCO^+ (white) emission. The positional uncertainty ellipses of the IRAS point source's IRAS 13547-3944 in CG 12-S and IRAS 13546-3941 in CG 12-N are also shown.

of the 3s factor is compact and lies on the outflow axis only $\sim 20''$ away from the apex of the NIR cone (Fig. 9), the putative position of the outflow driving source. This suggests, that the high 3s C^{18}O line intensities and the molecular outflow could be connected.

6.2.2. CG 12-N

PMF produces a seemingly straightforward solution for CG 12-N. However, the available data from molecules other

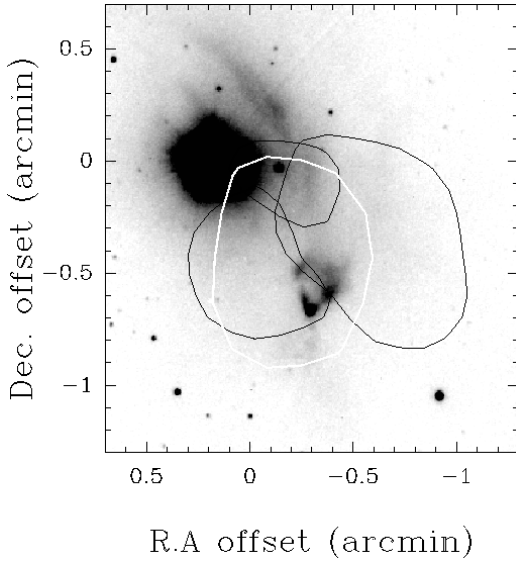


Fig. 10. The CG 12-S $C^{18}O$ (2–1) 1s, 2s, and 3s (from East to West) factor peak emission positions (0.8 K km s^{-1} contours) and DCO^+ core position (white) superposed on the SOFI K_s band image. Offsets from the map’s zero position are shown in arcminutes. The SEST beam at the $C^{18}O$ (2–1) frequency is 0.37 arcmin .

than $C^{18}O$ and the 1.2 mm continuum emission deny such a simple solution. As argued in Sect. 6.1, it is likely that the cloud component traced by DCO^+ and N_2H^+ is heavily depleted. If this is the case, $C^{18}O$ only probes the undepleted part of CG 12-N.

6.3. Clouds’s physical properties

A straightforward division of the CG 12 molecular cloud into three homogeneous components, CG 12-N, CG 12-S, and CG 12-SW, is not possible. The good velocity resolution and the high signal-to-noise ratio of the data allows one to divide the $C^{18}O$ data into separate components. However, the derivation of the cloud or core physical properties calls for a detailed three-dimensional non-LTE model that accounts for both the molecular depletion, the varying density, and excitation conditions. Such a model is beyond the scope of this paper and will be left for the future. The LTE-approximation approach is used instead of a sophisticated model to make a zeroth-order estimate of the masses of the three $C^{18}O$ maxima, CG 12-N, CG 12-S, and CG 12-SW. An average $C^{18}O$ excitation temperature for each maximum is estimated using the observed relative $C^{18}O$ (2–1) and (1–0) line intensities.

6.3.1. Mass and column-density estimation

The observed T_A^* line temperatures were converted into main beam temperatures using the beam efficiencies in Table 1. The $C^{18}O$ excitation temperatures were estimated from the $C^{18}O$ (1–0) and (2–1) data by assuming optically thin $C^{18}O$ emission and LTE. This assumes that the observed emission in both transitions originates in the same volume of gas at a constant excitation temperature. The observed $C^{18}O$ line $T_{MB}(2-1)/T_{MB}(1-0)$ ratio is 1.8 in CG 12-S, compatible with an excitation temperature near 15 K. In CG 12-N and CG 12-SW, this ratio is one or less, indicating excitation temperatures of the order of 10 K.

The masses of CG 12-N, CG 12-S, and CG 12-SW are calculated without dividing them into smaller components. The

spectra between declination offsets (including the limits) $-120''$ and $+60''$ were assigned to CG 12-S. The spectra above and below these limits were assigned to CG 12-N and CG 12-SW, respectively. An average $C^{18}O$ excitation temperature of 10 K is now assumed for CG 12-N and CG 12-SW and 15 K for CG 12-S. The adopted $C^{18}O$ abundance is 2.0×10^{-7} . This results in calculated total masses of 34, 96, and $110 M_\odot$ for CG 12-SW, CG 12-S and CG 12-N, respectively, when $C^{18}O$ (1–0) data is used. If $C^{18}O$ (2–1) data is used the masses are 14, 49, and $53 M_\odot$. The maximum T_{MB} line integrals can be used to estimate the H_2 column densities in the corresponding beams. The calculated maximum column densities in the $C^{18}O$ (1–0) beam are 1.3×10^{22} , 1.8×10^{22} , and $2.7 \times 10^{22} \text{ cm}^{-2}$ for CG 12-SW, CG 12-S, and CG 12-N, respectively. For the $C^{18}O$ (2–1) beam the corresponding values are 6.4×10^{21} , 1.6×10^{22} , and $1.8 \times 10^{22} \text{ cm}^{-2}$.

The masses calculated from the $C^{18}O$ (1–0) data are approximately twice higher than from the (2–1) data. The LTE approximation assumes that all the $C^{18}O$ rotational states are thermalized. However, according to Warin et al. (1996) only the lowest $C^{18}O$ rotational state is thermalized in dark clouds, and the higher states are subthermally excited. The subthermal excitation would be stronger in the relatively low-density cloud envelope than in the dense core. The subthermal level population leads to an underestimation of the cloud mass when calculated from the $C^{18}O$ (2–1) data. This could be a partial explanation for the large discrepancy between the masses calculated using $C^{18}O$ (1–0) and (2–1) data.

Strong $C^{18}O$ (3–2) emission (maximum $T_{MB} \sim 11 \text{ K}$) distributed in a similar way to the 3s PMF factor was detected by Haikala et al. (2006) in the centre of CG 12-S. The $C^{18}O$ (3–2) data was modelled with a compact ($60''$ to $80''$ diameter) and hot ($80 \text{ K} \lesssim T_{ex} \lesssim 200 \text{ K}$) optically-thin clump of $\sim 1.6 M_\odot$. The high temperature was derived from the $T_{MB}(C^{18}O(3-2))/T_{MB}(C^{18}O(2-1))$ ratio. However, the $T_{MB}(C^{18}O(2-1))/T_{MB}(C^{18}O(1-0))$ ratio for the CG 12-S PMF factor 3s is not compatible with such a high temperature. This could be due to, e.g., contribution from a subthermally excited cool cloud envelope to the $C^{18}O$ (1–0) emission. The LTE mass calculated from the $C^{18}O$ (2–1) 3s component within the area modelled in Haikala et al. (2006) is $4.1 M_\odot$ when a T_{ex} of 15 K is assumed. The discrepancy in the calculated excitation temperatures and masses highlights the uncertainties when LTE approximation is used and only data of the two lowest $C^{18}O$ transitions are available. In contrast to CG 12-S, the $C^{18}O$ T_{ex} and the LTE mass of CG 12-N correspond well to the modelled values using the three transitions (Haikala et al. 2006).

6.4. Summary

The analysis of the spectral lines presented above deliver a complicated picture of CG 12. Even though the spectral lines are relatively narrow, the analysis reveals a rich structure in line shape and velocity. Probable depletion of molecules on dust grains in CG 12-N further complicates the interpretation. The cloud parameters derived using the LTE analysis are highly uncertain. However, if the molecular-line observations are combined with the available optical, NIR, FIR, and mm continuum data, the cloud structure can be discussed with some confidence.

6.4.1. CG 12-N

CG 12-N harbours a compact, cold mm source, and the detected relatively weak molecular emission in high-density tracers is

probably associated with this source. Much of the molecular material associated with this cloud component is likely to be highly depleted onto dust. The observed strong $C^{18}O$ emission towards CG 12-N therefore originates in the envelope of this depleted core or in a separate entity seen in the same line of sight. The ^{12}CO observed in the direction of CG 12-N has line-wing emission indicating molecular outflow. It is not known if this outflow is connected to the outflow in CG 12-S or if it is local and originates in CG 12-N.

6.4.2. CG 12-S

The bulk of the observed $C^{18}O$ emission does not trace the gas associated with the compact cloud core detected in $H^{13}CO^+$, DCO^+ and CS (3–2) lines. Most likely the $C^{18}O$ emission traces only the surface of this core. The moderate $C^{18}O$ line wing emission, probably due to interaction of the highly collimated molecular outflow with the surrounding gas, complicates the interpretation even further.

The molecular line data presented in this paper, combined with the molecular outflow data from White (1993), the NIR imaging, and mm dust continuum data (Haikala 2007, in preparation), shows that the outflow centre coincides with the mm continuum source and the NIR cone in the centre of the DCO^+ core. The strong point source IRAS 13547–3944 is offset from the mm source and from h4636. This point source could, however, be the driving source for the strong redshifted outflow lobe north of CG 12-S.

6.4.3. CG 12-SW

CG12-SW is inconspicuous when compared to the two stronger $C^{18}O$ maxima. No signs of star formation have been found in its direction, and it is therefore either still in pre-star formation phase or its density-temperature structure is such that no star formation will take place. The arc-like feature that connects CG 12-S and CG 12-SW at velocities from -6.6 km s^{-1} to -6.2 km s^{-1} in Fig. 11 suggests that CG 12-SW might be related to CG 12-S.

7. Conclusions

We have performed a detailed, high signal-to-noise ratio, mm-line study of CG 12 in various molecular transitions, principally of $C^{18}O$ (1–0) and $C^{18}O$ (2–1), as well as in molecular lines probing dense material, with the following results:

1. The $C^{18}O$ line emission is distributed in a 10' North-South elongated lane with two strong, compact maxima, CG 12-N and CG 12-S, and a weaker maximum, CG 12-SW.
2. High-density tracers CS (2–1), (3–2), DCO^+ , and $H^{13}CO^+$ are detected in both strong $C^{18}O$ maxima. Emission from these molecules is weak in CG 12-N, but in CG 12-S it defines a compact core (referred to as DCO^+ core) that is spatially offset from the $C^{18}O$ maximum.
3. The emission from the high-density tracers in CG 12-N takes place at a velocity where emission from $C^{18}O$ is weak. The molecules associated with the cloud component detected in high-density tracers are likely to be heavily depleted.
4. Positive matrix factorization was applied to study the cloud $C^{18}O$ fine-scale structure. The observed strong $C^{18}O$ emission in CG 12-N (PMF factor 2n) originates in the envelope of the depleted cloud component or in a separate entity seen in the same line of sight. In CG 12-S the most intense PMF factor 3s traces warm gas on the surface of the DCO^+ core or a separate adjacent cloud component.
5. The driving source of the collimated molecular outflow detected by White (1993) lies in the DCO^+ core.
6. The average $C^{18}O$ LTE mass is $\sim 80 M_{\odot}$ for CG 12-N, $\sim 70 M_{\odot}$ for CG 12-S, and $\sim 20 M_{\odot}$ for CG 12-SW. These numbers can only be considered as a zeroth-order estimate because of the uncertainty in defining the $C^{18}O$ excitation temperature and possible molecular depletion in the $C^{18}O$ maxima.
7. If the distance to CG 12, 630 pc, is correct, the linear size and the mass of this cometary globule approaches that of a typical low-mass star-forming region like e.g. Chamaeleon I.

Acknowledgements. We thank Bo Reipurth for critically reading the manuscript and for very useful comments that helped to improve this paper. We also thank Mika Juvela and Kalevi Mattila for helpful discussions and Pentti Paatero for providing the PMF code. Data retrieved from the Canadian Astronomy Data Centre were used to produce the CO outflow contours in Fig. 9. The Canadian Astronomy Data Centre is operated by the Herzberg Institute of Astrophysics, National Research Council of Canada.

References

- Arnal, E. M., Bajaja, E., Larrarte, J. J., Morras, R., & Pöppel, W. G. L. 2000, *A&AS*, 142, 35
- Haikala, L. K., Harju, J., Mattila, K., & Toriseva, M. 2005, *A&A*, 431, 149
- Haikala, L. K., Juvela, M., Harju, J., et al. 2006, *A&A*, 454, L71
- Hartman, D., & Burton, W. B. 1997, *Atlas of Galactic Neutral Hydrogen* (Cambridge University Press)
- Hawarden, T. G., & Brand, P. W. J. L. 1976, *MNRAS*, 175, 19P
- Herbst, E. 1982, *A&A*, 111, 76
- Herschel, J. F. W. 1847, *Results of Astronomical Observations made during the years 1834, 5, 6, 7, 8 at the Cape of Good Hope* (London: Smith, Elder)
- Juvela, M., Lehtinen, K., & Paatero, P. 1996, *MNRAS*, 280, 616
- Kalberla, P. M. W., Burton, W. B., Hartman, D., et al. 2005, *A&A*, 440, 775
- Maheswar, G., Manoj, P., & Bhatt, H. C. 2004, *MNRAS*, 355, 1272
- Odenwald, S. F. 1988, *ApJ*, 325, 320
- Rawlings, J. M. C., Taylor, S. D., & Willimas, D. A. 2000, *MNRAS*, 313, 461
- Reipurth, B. 1983, *A&A*, 117, 183
- Reipurth, B., Nyman, L.-Å., & Chini, R. 1996, *A&A*, 314, 258
- Rohlfs, K., & Wilson, T. L. 1999, *Tools of Radio Astronomy* (Berlin: Springer)
- Russeil, D., Juvela, M., Lehtinen, K., Mattila, M., & Paatero, P. 2003, *A&A*, 409, 135
- Tafalla, M., Myers, P. C., Caselli, P., Walmsley, C. M., & Conito, C. 2002, *ApJ*, 569, 815
- Santos, N. C., Yun, J. L., Santos, S. A., & Marreiros, R. G. 1998, *AJ*, 116, 1376
- Warin, S., Benayoun, J. J., & Viala, Y. P. 1996, *A&A*, 308, 535
- White, G. 1993, *A&A*, 274, L33
- Williams, P. M., Brand, P. W. J. L., Longmore, A. J., & Hawarden, T. G. 1977, *MNRAS*, 181, 179
- Yonekura, Y., Hayakawa, T., Mizuno, N., et al. 1999, *PASJ*, 51, 837

Online Material

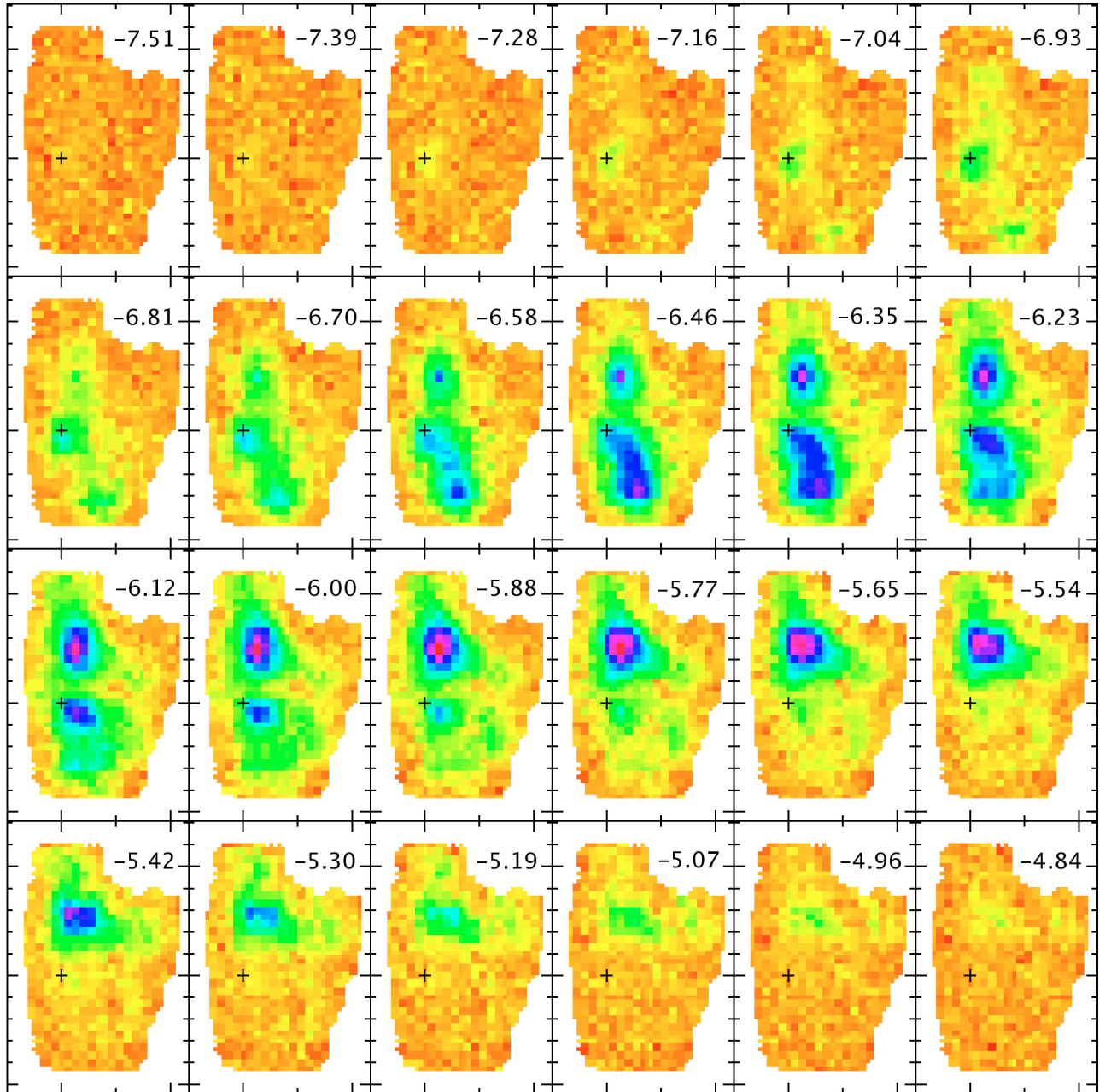


Fig. 11. T_A^* channel map of the $C^{18}O$ (1–0) emission in CG 12. The LSR velocity is indicated in the upper right corners of the panels. Each pixel corresponds to a single observed position. The highest intensity in the panels is ~ 3.0 K. The cross in the panels is located in the map's centre position, $13^{\text{h}}57^{\text{m}}43^{\text{s}}.1, -39^{\circ}58'43''.3$ (J2000).

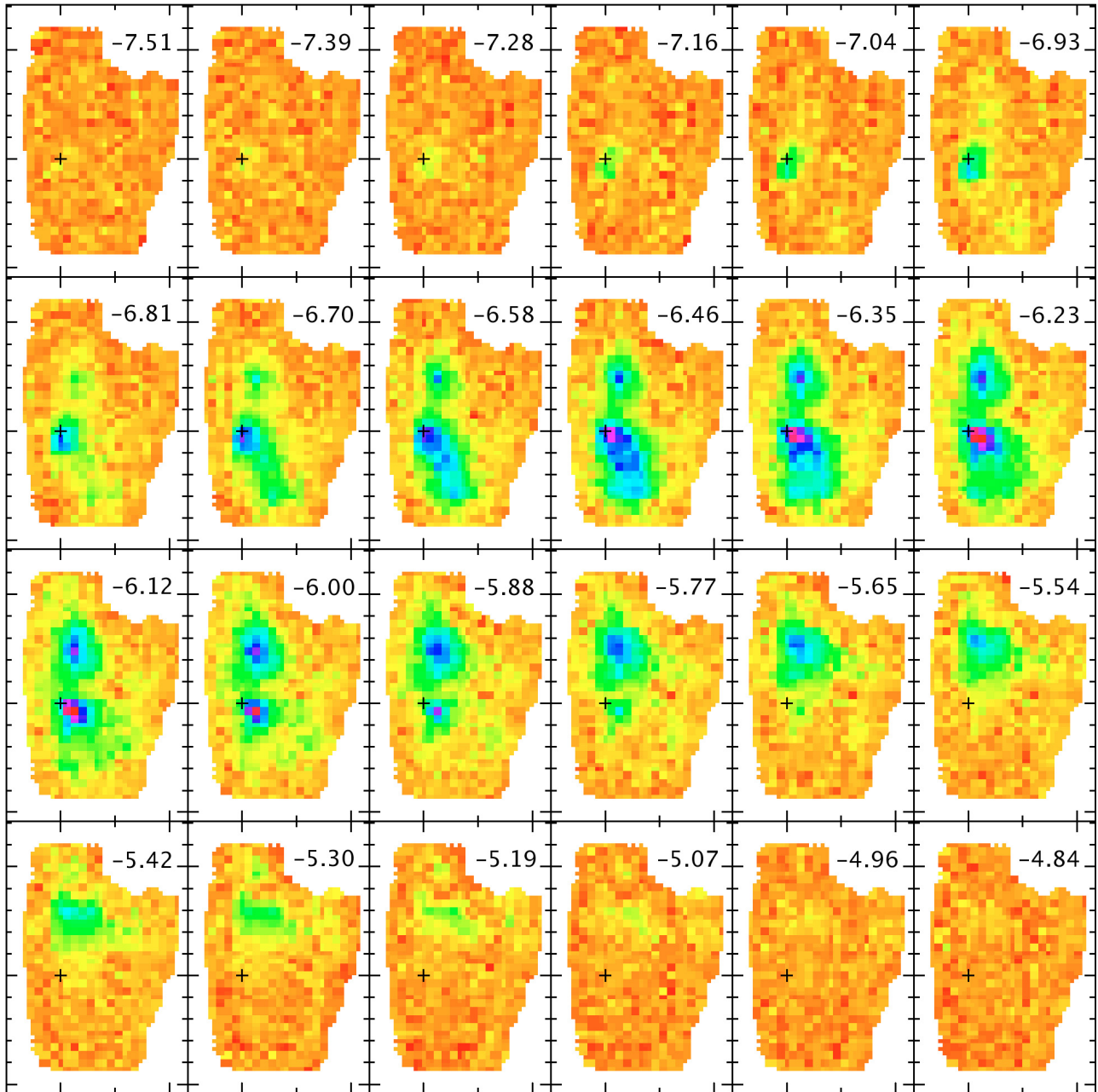


Fig. 12. As Fig. 11 but for the $C^{18}O$ (2-1) transition. The data shown in the figure is binned to the same channel width as the (1-0) data, 0.116 km s^{-1} . The colour scale is the same as in Fig. 11.

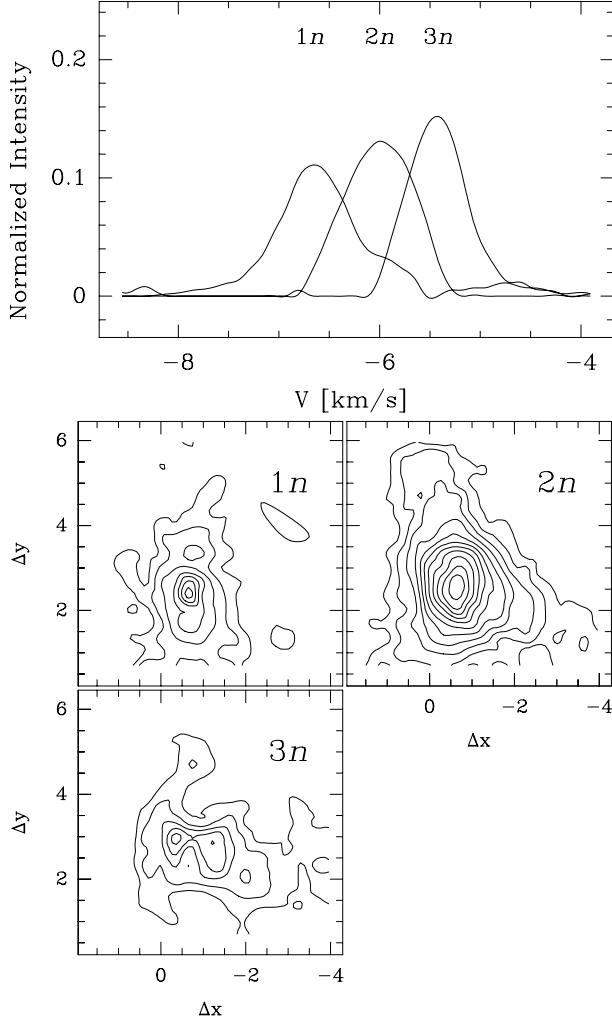


Fig. A.1. Upper ccc panel: the basic spectral profiles (factors) calculated by the PMF in CG 12-N (three factor fit), $C^{18}O$ (1–0) data. Lower panels: maps of the weights of the basic factors. The lowest contour level and increment are 0.2 K km s^{-1} . Offsets from the centre position of the original $C^{18}O$ map are shown in arcminutes on the x and y axes.

Appendix A: Positive matrix factorization analysis of CG 12

A.1. CG 12-N

The results of the PMF, assuming three factors, to observed $C^{18}O$ (1–0) and (2–1) data in CG 12-N are shown in Figs. A.1 and A.2. The uppermost panels show the three fitted PMF factors. The area under each factor is normalized to one. The histogram superposed on the rightmost factor in Fig. A.2 indicates the velocity resolution of the input data. The intensity distribution of the PMF factors in CG 12-N is shown in the lower three panels.

The PMF reproduces the velocity structure displayed in Figs. 11 and 12 well. The fits to the $C^{18}O$ (1–0) and (2–1) data are independent of each other. Therefore it is encouraging that the PMF output factors for both $C^{18}O$ transitions are similar in velocity and in spatial distribution. Because of the unambiguity of the fits for both transitions the factors, centred at -6.6 , -5.9 and -5.4 km s^{-1} , are referred to in the following as $1n$, $2n$, and $3n$, respectively.

The PMF factors, $1n$, $2n$, and $3n$, are distributed in a north-south oriented ridge, in a pear-shaped body and a narrow

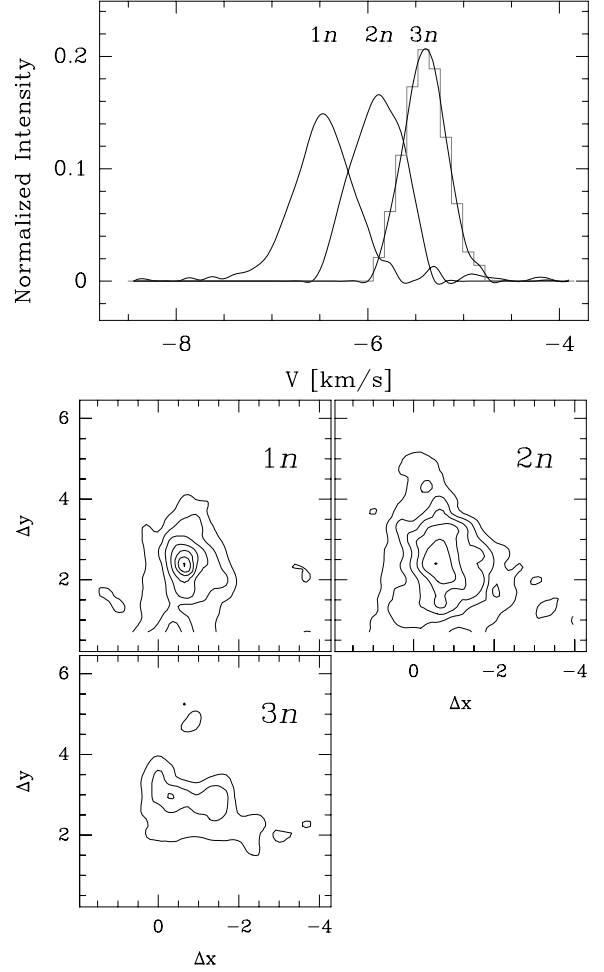


Fig. A.2. As Fig. A.1 but for $C^{18}O$ (2–1) data. Factor $3n$ in the upper panel has been plotted also as a histogram to indicate velocity resolution of the input/output spectra.

east-west ridge, respectively. The $3n$ factor lies at the velocity where the emission from the $H^{13}CO^+$, DCO^+ , and N_2H^+ is at its maximum. Even though this factor is not readily evident in the individual spectra, PMF finds it in both $C^{18}O$ transitions. Factors $2n$ and $3n$ are symmetric, but factor $1n$ has blue and redshifted wing-like emission, especially in the (1–0) transition. According to the PMF fit the high $T_A^*(C^{18}O(1-0))/T_A^*(C^{18}O(2-1))$ ratio observed in the direction of CG 12-N is due to the factor $2n$.

If the number of factors in the PMF is chosen to be four, PMF divides in essence the factor $1n$ into two, leaving the two other factors untouched. The spatial distribution of the split-up factors is similar to that of the $1n$ in the three-factor PMF. If the number of factors is increased further to five, the result is similar to that with four factors, plus a fifth factor which has nearly zero intensity, “empty” field, in the map. The three factors are therefore sufficient to produce the velocity structure evident in Fig. 11, and increasing the number of factors does not improve the fit significantly.

A.2. CG 12-S and CG 12-SW

The results of the PMF fits, assuming four factors, to both observed $C^{18}O$ transitions in CG 12-S are shown in Figs. A.3 and A.4. The location of the DCO^+ core is shown with a dashed

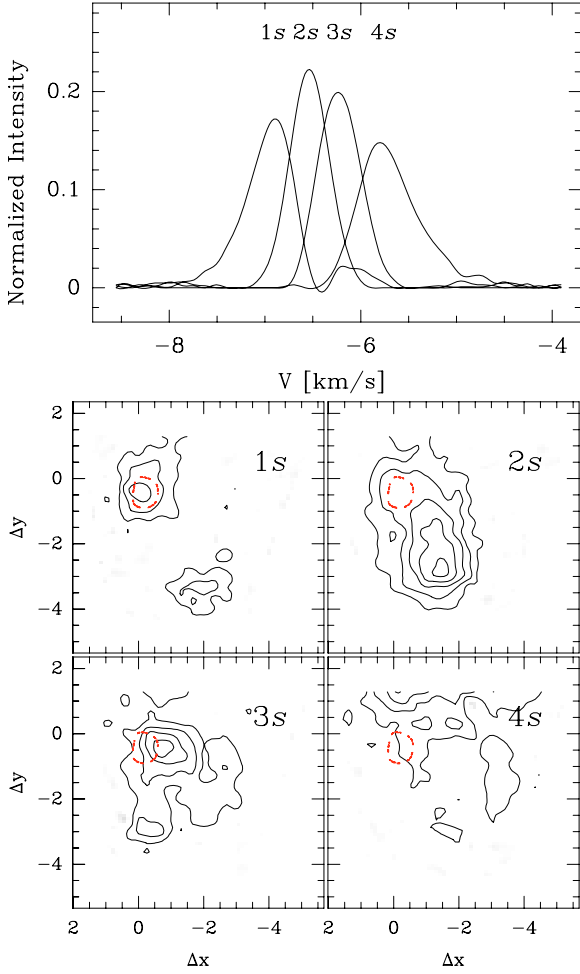


Fig. A.3. *Upper panel:* the basic spectral profiles calculated by the PMF in CG 12-S (four factor fit), $C^{18}O$ (1–0) data. *Lower panels:* the maps of the intensity of the basic factors. The factor numbers correspond to the numbers in the upper panel. The lowest contour level and increment is 0.2 K km s^{-1} . The dashed contour outlines the DCO^+ core.

contour in the figures. The factors, centred at -6.8 , -6.4 , -6.2 , and -5.8 km s^{-1} , will be referred to as 1s to 4s, respectively.

The most redshifted factor 4s covers the very northern part of the region, and is close in velocity to the $2n$ factor in CG 12-N. It is natural to consider that this factor is due to emission extending from CG 12-N to CG 12-S. Also the very faint emission observed in the northern part of the field in other three factors is at least partly due to emission from CG 12-N.

The emission from the most blueshifted factor 1s is concentrated just below the (0,0) position. The 2s factor represents the arc which connects CG 12-S and CG 12-SW (Fig. 11). There is a small size, local maximum in the $C^{18}O$ (2–1) 2s factor north of the DCO^+ core. Even though this local maximum is not seen in the $C^{18}O$ (1–0) 2s factor, there is extended emission at its location. The southern part of the arc is more intense in the (1–0) transition than in the (2–1). The maximum of the southern extension coincides with CG 12-SW. The emission from the 3s factor peaks west of the DCO^+ core, and is seen in both transitions.

A.3. Individual line profiles

The PMF fits to the $C^{18}O$ lines in the same selected positions as in Fig. 5, are shown in Fig. A.5. The residuals obtained by subtracting the added up PMF factors from the observed lines are

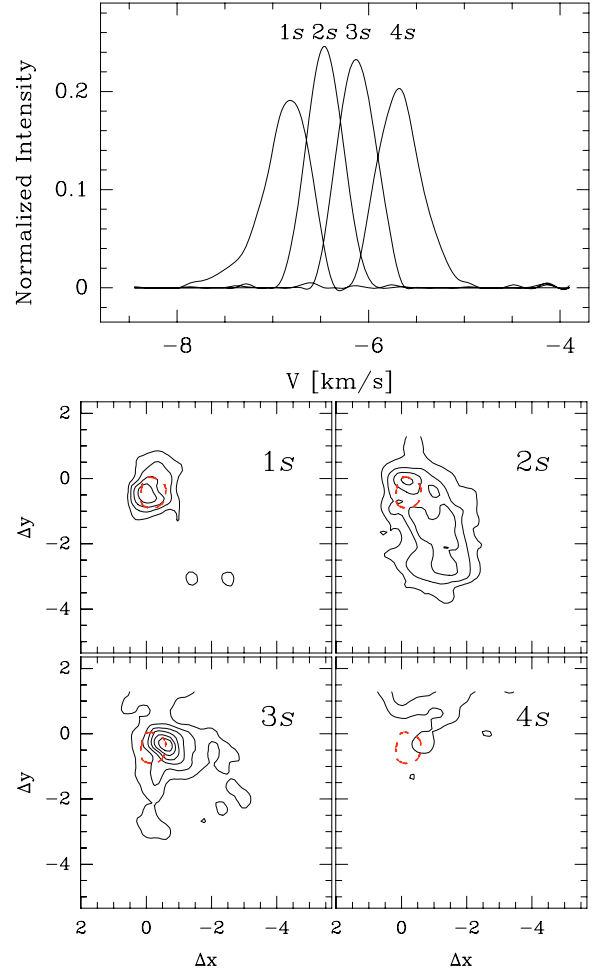


Fig. A.4. As Fig. A.3 but for $C^{18}O$ (2–1) data.

shown below the lines in the figure. A grey scale map of all the PMF fit residuals is shown in Fig. A.6. One should stress that, unlike a Gaussian multicomponent fit to a single spectrum, PMF fits, in this case 3 (CG 12-N) or 4 (CG 12-S) factors into all the input spectra simultaneously. Neither the shape nor the velocity of the factors is fixed in the fit. The two $C^{18}O$ transitions were fit separately, and PMF could have used factors differing in profile and velocity for the two transitions. The fitted PMF factors are, however, similar both in shape and velocity. The residuals shown in Figs. A.5 and A.6 are small, and demonstrate that PMF produces a good fit to the data.

The largest residual in Fig. A.5 takes place in the blue shifted side of the $C^{18}O$ (1–0) line in the centre of CG 12-N (position $-40''$, $160''$). This would imply that the blue shifted wing of factor $C^{18}O$ (1–0) 1n is too strong. A closer comparison of the input data and PMF results reveals that similar deviations take place for three other $C^{18}O$ (1–0) spectra around the position above. The $C^{18}O$ (1–0) line profiles farther away from the CG 12-N centre actually do have a more prominent blue shifted wing than the four above mentioned spectra. The large number of spectra with good fits outweighs the less optimal fit for the spectra in the centre of CG 12-N. The residuals shown in Fig. A.5 for the remaining four spectra in CG 12-S are smaller than in position $(-40''$, $160'')$.

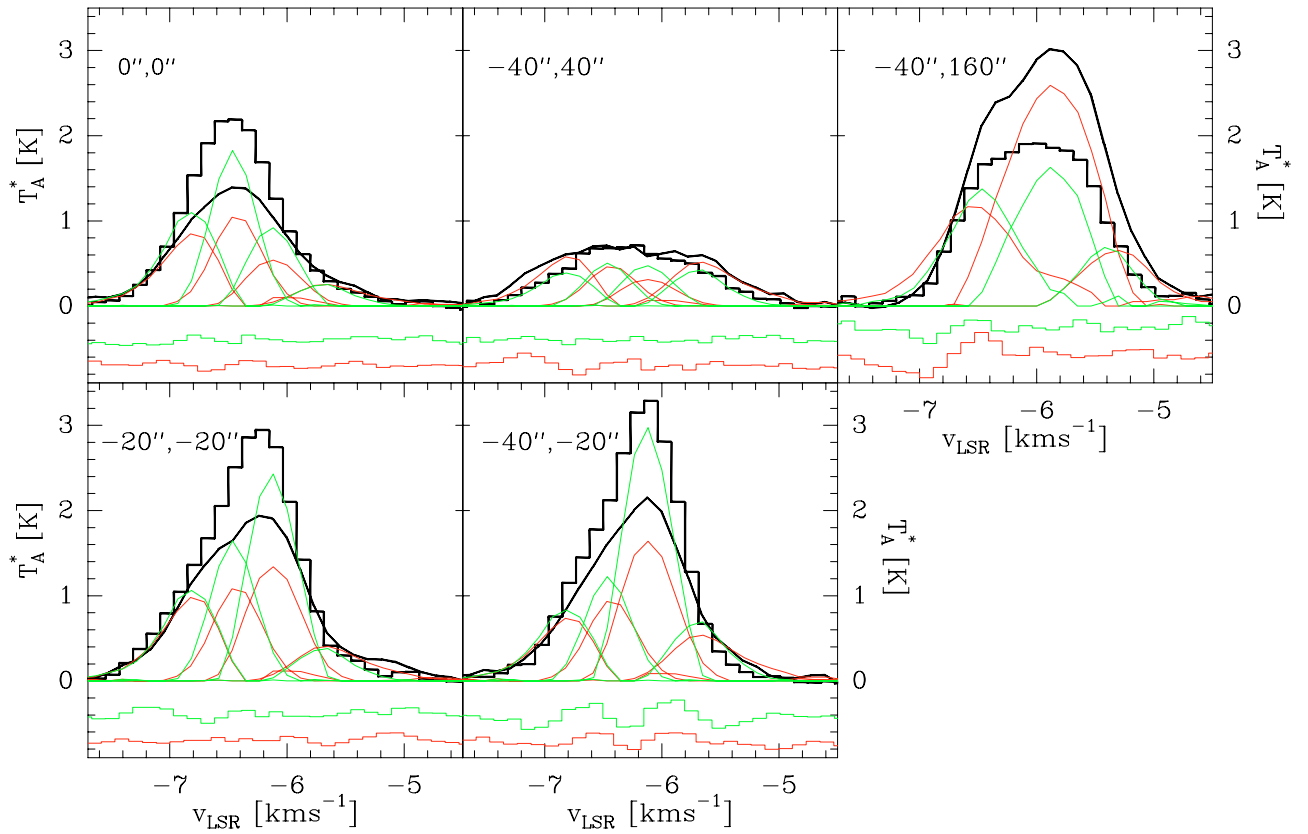


Fig. A.5. The PMF fit to the $C^{18}O$ lines in the selected positions in Fig. 5. The observed $C^{18}O$ (2–1) and (1–0) lines are plotted with a heavy histogram and line, respectively. The green and red lines show the fitted PMF $C^{18}O$ (2–1) and (1–0) factors, respectively. The residuals of the fits are shown in the lower part of each panel.

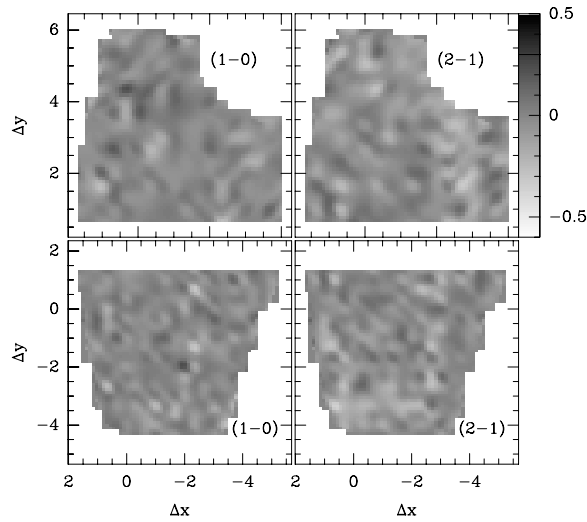


Fig. A.6. The PMF fit residuals in the $K \text{ km s}^{-1}$ scale.